Wave-like Patterns in Precessing Elliptical Rings for Swarming Systems

Ming Xu [1,2,†] and **Colin R McInnes** [2,‡]

[1] *Beihang University, Beijing 100191, China;* [2] *University of Glasgow, Glasgow G12 8QQ, UK*

A continuum model for a swarm of devices is investigated with the devices moving along precessing elliptical Earth-centred orbits. Wave-like patterns in these precessing elliptical rings with peaks in swarm density are found which can be used to provide enhanced coverage for Earth observation and space science. Two orbital models are considered for the purpose of comparison; perturbed by J_2 and solar radiation pressure, and perturbed by J_2 and J_3 respectively, each with a different frozen eccentricity. By removing osculating orbital elements, only the long-period orbit eccentricity and argument of perigee are chosen to derive closed-form solutions to the continuum model for the swarm density. Zero-density lines in the swarm density are found, as well as infinite density at certain boundaries. Comparison between the analytic and numerical number density evolution is made to yield the range of applicable eccentricity based the maximum error tolerance, as well as the minimum number of swarm members required to approximate continuous evolution. Closed-form solutions are then derived to predict the number density of swarm devices for magnetic-tail measurement and Earth observation applications.

Nomenclature

n	=	analytic swarm number density solution
J_2	=	second zonal coefficient of Earth's gravitational field
J_3	=	third zonal coefficient of Earth's gravitational field
e	=	long-periodic eccentricity
ω	=	long-periodic argument of perigee

† Associate professor, School of Astronautics; currently China Scholarship Council Research Fellow, School of Engineering, University of Glasgow; xuming@buaa.edu.cn.

‡ James Watt Chair, Professor of Engineering Science, School of Engineering, colin.mcinnes@glasgow.ac.uk.

$\bar{e}$	=	mean eccentricity
e_f	=	frozen eccentricity
$\bar{\omega}$	=	mean argument of perigee
R_e	=	Earth's radius
a	=	orbit semi-major axis
i	=	orbit inclination
μ_{Earth}	=	gravitational parameter of Earth
ϕ	=	pericentre angle between the Sun-Earth line and the pericentre of the elliptical orbit
t	=	time
n_{Sun}	=	angular rate of the Earth around the Sun
c_R	=	reflectivity coefficient of the spacecraft, chosen as 1.8
m	=	mass of the spacecraft
A	=	effective area exposed to the Sun
$\boldsymbol{v}$	=	velocity vector of a single device
N	=	total number of swarm devices
Θ	=	angle used to replace the time term in all relevant equations for simplicity
n'	=	numerical swarm number density solution
ε	=	relative errors of the analytic and numerical number density solutions
r_a^{crital}	=	critical radius for measuring deep magnetic tail or obtaining high resolution images
$r_a^{\max}$	=	maximum radius restricted by the communications link budget
n_{Sun}	=	angular rate of the Earth around the Sun

I. Introduction

Elliptical orbits are of interest for applications such as Molniya-like orbits and 'magic orbits' [1], and have been considered for swarm applications for telecommunications and Earth observation services [2-4]. Moreover, high area-to-mass ratio satellites strongly perturbed by solar radiation pressure have also been considered for forced orbit precession of elliptical orbits, again to deliver novel telecommunication and Earth observation services [5]. However, unlike the

discrete structure of constellations with a modest number of satellites, large constellations of Cubesats or 'Chipsats' exhibit a fluid-like continuum behaviour [6,7]. Therefore, rather than using ordinary differential equations (ODE) to propagate the motion of each member of the constellation, a continuum approach is employed in this paper to model the evolution of large numbers of small 'smart-dust-type' devices using partial differential equations (PDE).

An initial application of the continuum approach in satellite astrodynamics was proposed by McInnes [8] for the evolution of debris clouds. Moreover, Gor'Kavyi et al. [9,10] used a continuum approach in orbital element space serving as a tool to analyse the transport of interplanetary dust grains as well as their long-term dynamical evolution. Later, considering both on-orbit failures and the deposition of new micro-satellites, McInnes [11] derived closed-form solutions to the PDE continuity equation based on the method of characteristics, which provided insights into the macroscopic dynamics of the problem and long-term, asymptotic behaviour. For pattern formation in elliptical rings, a wave-like pattern was found from a set of closed-form solutions to the continuity equation. In principle, the resulting density peaks could provide enhanced coverage [2]. Letizia et al. [12] summarized applications of the continuity equation approach, including interplanetary dust [9], nanosatellites [11] and high area-to-mass SpaceChips [13] and developed a standard procedure for the analytic solution to the continuity equation in orbital element space. McInnes [14] studied the evolution of the density of swarms of self-propelled devices in heliocentric orbit with closed-form solutions developed analytically for several scenarios, such as the evolution of an infinite sheet or a finite disk, with on-orbit failures, and with the constant disposition of new devices at one boundary.

As an extension of McInnes and Colombo [2], the continuum method is used in this paper to investigate the evolution of the number density of a swarm of devices on perturbed, precessing elliptical orbits. Firstly, by removing osculating terms, the simplified dynamics of the long-period eccentricity and argument of perigee angle are considered for J_2 and solar radiation pressure (SRP) perturbations, as well as long-period eccentricity and argument of perigee angle dynamics for J_2 and J_3 perturbations. Then, a number of initial swarm density distributions are modelled through the orbit eccentricity and argument of perigee angle for the two perturbed precessing elliptical orbit models noted above. The closed-form solutions to these distributions are then derived by the method of characteristics. Finally, by integrating the swarm number density, the number of swarm devices available to provide in-situ observations for magnetic-tail and Earth imaging missions are investigated.

II. Orbital Evolution Models of Precessing Elliptical Rings

A. *Precessing Elliptical Orbit Perturbed by J_2 and J_3*

For a precessing elliptical orbit perturbed by the Earth's oblateness, the evolution of the eccentricity e and argument of perigee ω are considered to be effected by the J_2 and J_3 terms of the zonal spherical harmonics. The components of the eccentricity vector (e_x, e_y) are defined as $e_x = e\cos\omega$ and $e_y = e\sin\omega$, shown in Fig.1.

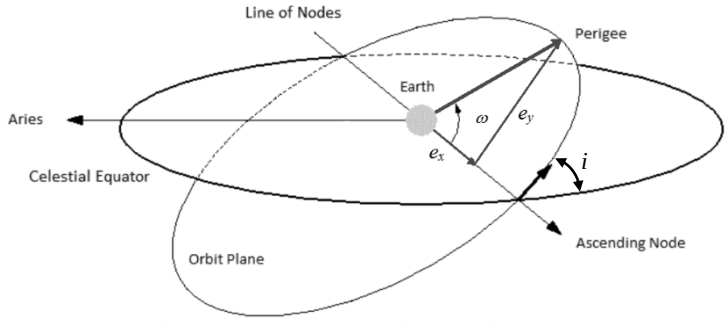

Fig.1 Geometry of elliptical orbit and the definition of (e_x, e_y).

According to perturbation theory [15], by removing osculating terms, the long-period evolution of the eccentricity vector (e_x, e_y) can be presented as

$$e_x = \bar{e}\cos\bar{\omega}\,,\ e_y = e_f + \bar{e}\sin\bar{\omega} \tag{1}$$

where $\bar{e}$ and $\bar{\omega}$ are the mean eccentricity and the mean argument of perigee defined by Kozai [15], and $e_f = -\frac{1}{2}\frac{J_3 R_e}{J_2 a}\sin i$ is the frozen eccentricity , R_e is the Earth's radius and a is the orbit semi-major axis. According to the classifications of short-period, long-period and secular terms by Kozai [15], the mean eccentricity $\bar{e}$ stays invariant and $\bar{\omega}$ has a secular perturbation with a linear rate given by

$$\dot{\bar{\omega}} = \frac{3}{2}J_2\frac{R_e^{\,2}}{a^2\left(1-\bar{e}^2\right)^2}\sqrt{\frac{\mu_{Earth}}{a^3}}\left(2-\frac{5}{2}\sin^2 i\right)+\sqrt{\frac{\mu}{a^3}}\frac{R_e^{\,4}J_2^2}{a^4\left(1-\bar{e}^2\right)^4}\left(\gamma_{0,0}+\gamma_{0,1}\sqrt{1-e^2}+\gamma_{0,2}\left(1-e^2\right)\right)+O\left(J_2^2\right) \tag{2}$$

where a is the orbit semi-major axis, i is the orbit inclination and μ_{Earth} is the gravitational parameter of Earth, and the coefficients $\gamma_{0,0}$, $\gamma_{0,1}$ and $\gamma_{0,2}$ can be found in Ref. [16]. Due to the existence of the frozen eccentricity, from Fig. 1, the actual eccentricity e and the actual argument of perigee ω have long-period terms depending on $\bar{\omega} = \bar{\omega}_0 + \dot{\bar{\omega}}\cdot t$, given by

$$\omega = \arctan\frac{\bar{e}\sin\bar{\omega}+e_f}{\bar{e}\cos\bar{\omega}} \tag{3}$$

$$e = \sqrt{\bar{e}^2\cos^2\bar{\omega}+\left(e_f+\bar{e}\sin\bar{\omega}\right)^2} = \bar{e}\sqrt{1+\hat{e}^2+2\hat{e}\sin\bar{\omega}} \tag{4}$$

where $\hat{e} = \frac{e_f}{\bar{e}}$ is defined as the equivalent eccentricity, and the mean argument of perigee $\bar{\omega}$ can be solved from Eq. (4) as

$$\bar{\omega} = \arcsin\left[\frac{1}{2\hat{e}}\left(\frac{e^2}{\bar{e}^2} - 1 - \hat{e}^2\right)\right] \tag{5}$$

The evolution of the actual eccentricity e and the actual argument of perigee ω are shown in Fig.2, where a series of mean eccentricities $\bar{e}$ 0.16×10^{-3}, 0.32×10^{-3}, 0.48×10^{-3}, 0.64×10^{-3} and 0.8×10^{-3} provide the initial conditions to create time-dependent functions e and ω. For an elliptical orbit with a given $\bar{e}$ and e_f, Eq. (3) can be rewritten as

$$\tan\omega\cos\bar{\omega} = \sin\bar{\omega} + \hat{e} \tag{6}$$

Therefore, $\bar{\omega}$ can be derived from ω based on Eq. (3) as

$$\bar{\omega} = \omega - \sin^{-1}(\hat{e}\cos\omega) \tag{7}$$

Substituting Eq. (7) into Eq. (4) formalises the mapping function F_{J_3} from ω to e as $e = F_{J_3}(\omega)$, and substituting Eq. (5) into Eq. (3) formalises the inverse mapping function $F_{J_3}^{-1}$ from e to ω as $\omega = F_{J_3}^{-1}(e)$.

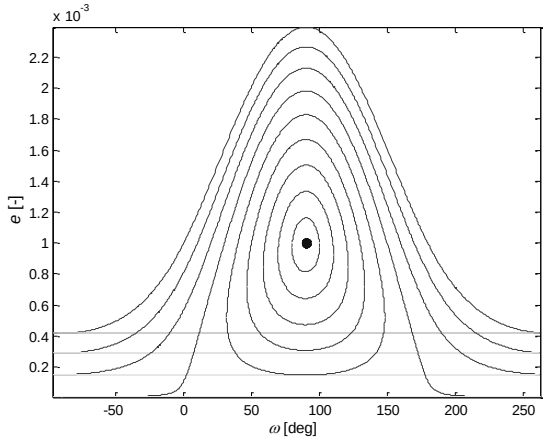

Fig.2 Evolution of the actual eccentricity and argument of perigee perturbed by J_2 and J_3: the mean semi-major axis is chosen to be 7178.137km and the mean inclination is 108^0, so that the frozen eccentricity is 0.001.

Differentiating Eq. (6) yields

$$\sec^2\omega\cdot\dot{\omega}\cdot\bar{e}\cos\bar{\omega} + \tan\omega\cdot\dot{\bar{e}}\left(-\sin\bar{\omega}\right)\cdot\dot{\bar{\omega}} = \dot{\bar{e}}\cos\bar{\omega}\cdot\dot{\bar{\omega}} \tag{8}$$

which can then be solved to obtain the derivative of ω as

$$\dot{\omega} = \dot{\bar{\omega}}\frac{\cos\omega}{\cos\bar{\omega}}\cos(\omega - \bar{\omega}) \tag{9}$$

Combining Eqs. (7) and (9) provides the 'velocity' of ω as

$$v_\omega(\omega)=\dot{\omega}=\dot{\bar{\omega}}\frac{\sqrt{1-\hat{e}^2\cos^2\omega}}{\sqrt{1-\hat{e}^2\cos^2\omega}+\hat{e}\sin\omega} \tag{10}$$

Then, differentiating Eq. (4) and then substituting Eq. (5) yields

$$v_e(e)=\dot{e}=\frac{\dot{\bar{\omega}}\bar{e}^2\hat{e}}{e}\cos\left(\sin^{-1}\left[\frac{1}{2\hat{e}}\left(\frac{e^2}{\bar{e}^2}-1-\hat{e}^2\right)\right]\right) \tag{11}$$

Both Eqs. (10) and (11) provide the 'velocities' of ω and e, i.e., v_ω and v_e, which can be used to obtain the characteristic functions of the continuity equation for the swarm density later in **Section III.A**.

Finally, Eqs. (3) and (4) define the J_2 and J_3 perturbations and can be considered as the linearized equation of the full dynamics near the frozen eccentricity e_f, which is derived in Refs. [16,17] as

$$\begin{cases}\dfrac{de}{dt}=-n\dfrac{R_e^4}{a^4}\dfrac{J_2^2}{\left(1-e^2\right)^3}\left(\dfrac{21}{16}-\dfrac{45}{32}\sin^2 i\right)e\cdot\sin^2 i\cdot\sin 2\omega \\ \dfrac{d\omega}{dt}=n\dfrac{R_e^2}{a^2}\dfrac{J_2}{\left(1-e^2\right)^2}\dfrac{3}{4}\left(4-5\sin^2 i\right)+n\dfrac{R_e^4}{a^4}\dfrac{J_2^2}{\left(1-e^2\right)^4}\left[\gamma_{0,0}+\gamma_{0,1}\sqrt{1-e^2}+\gamma_{0,2}\left(1-e^2\right)+\left(\gamma_{2,0}+\gamma_{2,2}\left(1-e^2\right)\right)\cos 2\omega\right]\end{cases} \tag{12}$$

where the coefficient $\gamma_{2,2}$ can be found in Ref. [16]. Thus, the linearized Eqs. (3) and (4) will be used to derive the analytic number density evolution in **Section III.B**, and the full dynamics from Eq. (12) will be used to implement the individual numerical evolution of swarm members in **Section. III.C**.

B. Precessing Elliptical Orbit Perturbed by J_2 and SRP

Considering the planar evolution of swarm members perturbed by the Earth's oblateness and solar radiation pressure (SRP) with the obliquity of the ecliptic ignored, another family of precessing elliptical orbits can be found, where the full orbital dynamics defined by $e_x=e\cos\phi$ and $e_y=e\sin\phi$, are given by the following [18-21]

$$\begin{cases}\dfrac{de_x}{dt}=n_{Sun}e_y\left(1-\dfrac{W}{\left(1-e_x^2-e_y^2\right)}\right) \\ \dfrac{de_y}{dt}=-n_{Sun}S\sqrt{1-e_x^2-e_y^2}-n_{Sun}e_x\left(1-\dfrac{W}{\left(1-e_x^2-e_y^2\right)}\right)\end{cases} \tag{13}$$

where e is the actual eccentricity, n_{Sun} is the angular rate of the Earth around the Sun, and ϕ is the actual pericentre angle between the Sun-Earth line and the pericentre of the elliptical orbit shown in Fig.3. Compared with Kozai's model [22] including only SRP and without the J_2 perturbation, the planar model used in this section includes both the SRP and J_2 terms, and has potential applications in orbit design for observations of the geomagnetic-tail.

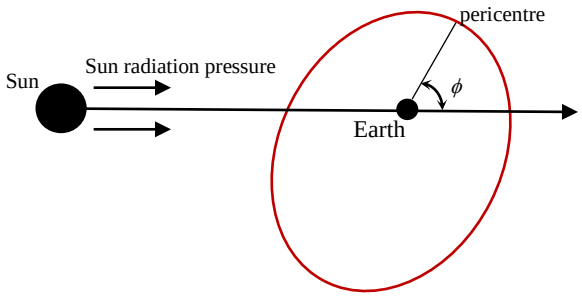

Fig.3 Geometry of precessing elliptical orbit and the definition of pericentre angle.

The solar radiation pressure parameter S and the oblateness parameter W are given by

$$\begin{cases} S = \dfrac{3}{2} a_{SRP} \dfrac{a^2}{\mu_{Earth}} \dfrac{\upsilon}{n_{Sun}} \\ W = \dfrac{3}{2} J_2 \dfrac{R_e^{\ 2}}{a^2} \dfrac{\upsilon}{n_{Sun}} \end{cases} \tag{14}$$

where $a_{SRP} = p_{SR} c_R A/m$ is the characteristic acceleration due to SRP, c_R is the reflectivity coefficient of the spacecraft, chosen as 1.8 in this paper and A is the effective area exposed to the Sun and m is the mass of the spacecraft that defines the area-to-mass ratio of the spacecraft as A/m. Moreover, R_e is again the mean Earth radius, a is the semi-major axis of the elliptic orbit, $\upsilon = \sqrt{\mu_{Earth}/a^3}$ is the mean orbital angular velocity of the orbit.

Eq. (13) governs the evolution of (e_x, e_y) and are non-integrable, but possess several equilibrium points including the frozen eccentricity (e_f, 0). These can be obtained from Eq. (13) and the following algebraic equation as

$$S\sqrt{1-e_f^2} + e_f\left(1 - \frac{W}{\left(1-e_f^2\right)}\right) = 0 \tag{15}$$

which can be approximated by ignoring higher order terms for small eccentricity, as

$$S\left(1+\tfrac{1}{2}e_f^2\right) + e_f\left(1 - W - 2e_f^2 \cdot W\right) = 0 \tag{16}$$

By the numerical investigation of the global evolution of the eccentricity vector, Colombo et al. [18] obtained different families of (e_x, e_y) which are considered to evolve around the equilibrium point (e_f, 0), as shown in Fig.4. Only the scenario with one equilibrium point is considered in this paper, and so the bifurcation case will be considered as future work.

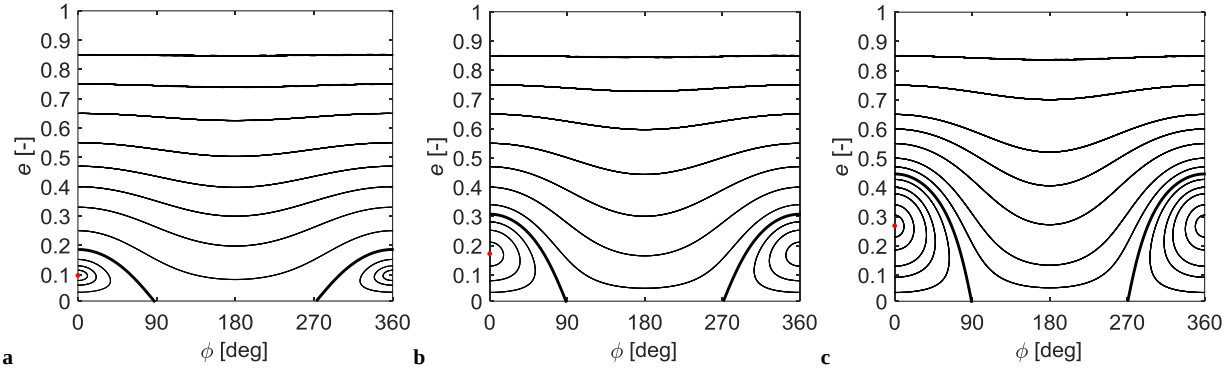

a **b** **c**

Fig.4 *e*-ϕ phase space evolution for high area-to-mass ratio spacecraft: **a** a=11,000km, A/m= 5m^2/kg; **b** a=11,000km, A/m= 10m^2/kg; **c** a=11,000km, A/m= 20m^2/kg.

To proceed with the analytic solution to Eq. (11), the simplified treatment developed in the classical perturbation theory of Kozai [15] is employed in the following section. Two new variables Δe_x and Δe_y are defined as the differences between (e_x, e_y) and the equilibrium point (e_f, 0) so that

$$\begin{cases} e_x = e_f + \Delta e_x \\ e_y = 0 + \Delta e_y \end{cases} \tag{17}$$

and are substituted into Eq. (14) to expand as a Taylor series, and then yield the linearized dynamics by ignoring high order terms in the expansion such that

$$\begin{cases} \Delta \dot{e}_x = n_{Sun} P \Delta e_y \\ \Delta \dot{e}_y = n_{Sun} Q - n_{Sun} R \Delta e_x \end{cases} \tag{18}$$

where $P = 1 - W - 2We_f^2$, $Q = -S\left(1 + \frac{1}{2}e_f^2\right) - \left(1 - W - 2We_f^2\right)e_f$, and $R = Se_f + 1 - W - 6We_f^2$, and Q is equal to 0 always due to the equilibrium point. Therefore, combining both these two equations from Eq. (18) it can be seen that

$$\Delta \ddot{e}_y + n_{Sun}^2 PR \cdot \Delta e_y = 0 \tag{19}$$

Hence, it is easy to solve for Δe_x and Δe_y from the above equation as

$$\begin{cases} \Delta e_x = \bar{e}\cos\bar{\phi} \\ \Delta e_y = \bar{e}\sin\bar{\phi} \end{cases} \tag{20}$$

where $\bar{e}$ and $\bar{\phi}$ are referred as the mean eccentricity and the mean angle related to the pericentre. $\bar{e}$ stays invariant which can be used to parameterize different families of (e_x, e_y), and $\bar{\phi} = \bar{\phi}_0 + \dot{\bar{\phi}}t$ with its linear rate given by

$$\dot{\bar{\phi}} = n_{Sun}\sqrt{PR} = n_{Sun}\sqrt{\left(1 - W - 2W \cdot e_f^2\right)\left(S \cdot e_f - 6W \cdot e_f^2 + 1 - W\right)} \tag{21}$$

Therefore, similar to the precessing elliptical orbit derived by Kozai [15], the eccentricity vector (e_x, e_y) evolves as

$$e_x = e_f + \bar{e}\cos\bar{\phi}\,,\ e_y = \bar{e}\sin\bar{\phi} \tag{22}$$

Besides, an equivalent eccentricity $\hat{e} = \frac{e_f}{\bar{e}}$ is defined for the precessing elliptical orbit as well. According to the definitions of e_x and e_y, the actual pericentre angle ϕ and the actual eccentricity can be written as

$$\phi = \arctan \frac{\bar{e} \sin \bar{\phi}}{e_f + \bar{e} \cos \bar{\phi}} \tag{23}$$

$$e = \sqrt{\left(e_f + \bar{e} \cos \bar{\phi}\right)^2 + \bar{e}^2 \sin^2 \bar{\phi}} = \bar{e} \sqrt{1 + \hat{e}^2 + 2\hat{e} \cos \bar{\phi}} \tag{24}$$

Based on Eq. (24) the mean argument of perigee $\bar{\phi}$ can then be solved from e as

$$\bar{\phi} = \cos^{-1}\left[\frac{1}{2\hat{e}}\left(\frac{e^2}{\bar{e}^2} - 1 - \hat{e}^2\right)\right] \tag{25}$$

Then, rewriting Eq. (23) as $e_f + \bar{e} \cos \bar{\phi} = \cot \phi \cdot \bar{e} \sin \bar{\phi}$ and differentiating yields

$$\bar{e}\left(-\sin \bar{\phi}\right) \cdot \dot{\bar{\phi}} = -\csc^2 \phi \cdot \dot{\phi} \cdot \bar{e} \sin \bar{\phi} + \cot \phi \cdot \bar{e} \cos \bar{\phi} \cdot \dot{\bar{\phi}} \tag{26}$$

Subsequently, the derivative of ϕ can be obtained as

$$\dot{\phi} = \dot{\bar{\phi}} \frac{\sin \phi}{\sin \bar{\phi}} \cos\left(\phi - \bar{\phi}\right) \tag{27}$$

For any family (e_x, e_y) parameterized by the mean eccentricity $\bar{e}$, the mean pericentre angle $\bar{\phi}$ can be solved from ϕ based on Eq. (23) as

$$\bar{\phi} = \phi + \sin^{-1}\left(\hat{e} \sin \phi\right) \tag{28}$$

which is substituted into Eq. (27) to obtain the derivative of the pericentre angle as

$$v_\phi(\phi) = \dot{\phi} = \dot{\bar{\phi}} \frac{\sqrt{1 - \hat{e}^2 \sin^2 \phi}}{\sqrt{1 - \hat{e}^2 \sin^2 \phi} + \hat{e} \cos \phi} \tag{29}$$

Then, differentiating Eq. (24) and substituting Eq. (25) into it yields

$$v_e(e) = \dot{e} = -\frac{\dot{\bar{\phi}} \bar{e}^2 \hat{e}}{e} \sin\left(\cos^{-1}\left[\frac{1}{2\hat{e}}\left(\frac{e^2}{\bar{e}^2} - 1 - \hat{e}^2\right)\right]\right) \tag{30}$$

Both Eqs. (29) and (30) provide the 'velocities' of ϕ and e, i.e., v_ϕ and v_e, which can then be used to obtain the characteristic functions of the continuity equation for the swarm density later in **Section III.B**.

Besides, substituting Eq. (28) into Eq. (24) formalises the mapping function G_{SRP} from ϕ to e as $e = G_{SRP}(\phi)$, and substituting Eq. (25) into Eq. (23) formalises the inverse mapping function G_{SRP}^{-1} from e to ϕ as $\phi = G_{SRP}^{-1}(e)$.

The linearized Eqs. (23) and (24) are used to derive the analytic number density evolution in **Section III.A**, and the full dynamics of Eq. (12) are used to implement the individual numerical evolutions of swarm members in **Section III.C**.

III. Continuum Models of Number Density for Precessing Elliptical Rings

By removing the short-period terms from the orbital elements, a single elliptical orbit with long-term precession is employed for a swarm of remote sensing satellites for Earth observation, or high area-to-mass ratio spacecraft for magnetic tail measurements. Different from classical orbital evolution formulated by an ordinary differential equation (ODE), the evolution of the swarm number density is modelled by a partial differential equation (PDE) as follows.

The short-period wave-like patterns investigated by McInnes and Colombo [2] were driven by a fast variable, i.e., the true anomaly of the unperturbed elliptic orbit, while here the swarm density is described by a slow variable. However, due to the mapping functions F_{J_3}, $F_{J_3}^{-1}$, G_{SRP} and G_{SRP}^{-1} between e and ϕ (or ω), only one variable will be selected for the continuum model. Thus, for both the J_2 and J_3 and the J_2 and SRP perturbation cases, four continuum models are considered based on the selected variable marked by a superscript as $n_{J_3}^{e}$, $n_{J_3}^{\omega}$, n_{SRP}^{e} and n_{SRP}^{ϕ}. Generally, the density is defined as the derivative of the number of swarm devices to the selected variable, for example as $n_{SRP}^{\phi}(\phi,t)=\frac{dN(\phi,t)}{d\phi}$ for an illustration, where N is the total number of swam devices.

Similar to treatments in fluid dynamics as well as the evolution of interplanetary dust [9,10], nano-satellite constellations [11], and heliocentric swarms [14], the continuum evolution of the swarm number density can be obtained by the follow PDE linking the swarm's density and a single device's velocity vector, as

$$\frac{\partial n}{\partial t}+\nabla\cdot(\boldsymbol{v}n)=0 \tag{31}$$

where n represents the swarm density, ∇ is the gradient operator on the selected variable of the precessing elliptical orbit and $\boldsymbol{v}$ is velocity vector of a single device parameterized by this variable.

A. Continuity Equation Modelled for J_2 and SRP Perturbations

For the J_2 and SRP perturbation case, the continuum evolution of the swarm density is written in terms of e and ϕ respectively as

$$\frac{\partial n_{SRP}^{e}}{\partial t}+v_e\frac{\partial n_{SRP}^{e}}{\partial e}+\frac{\partial v_e}{\partial e}n_{SRP}^{e}=0 \tag{32a}$$

$$\frac{\partial n_{SRP}^{\phi}}{\partial t}+v_\phi\frac{\partial n_{SRP}^{\phi}}{\partial \phi}+\frac{\partial v_\phi}{\partial \phi}n_{SRP}^{\phi}=0 \tag{32b}$$

The closed-form solution to Eqs. (32a) and (32b) is derived using the method of characteristics, as used by McInnes [11,14], McInnes and Colombo [2] and Letizia et al. [12]. Along the characteristic curves, the partial differential equation degenerates into two ordinary differential equations defined by Murphy [23] such that

$$\frac{d\phi}{dt} = v_\phi \tag{33}$$

$$\frac{de}{dt} = v_e \tag{34}$$

$$\frac{dn^{\phi}_{SRP}}{d\phi} + \frac{1}{v_\phi}\frac{\partial v_\phi}{\partial \phi} n^{\phi}_{SRP} = 0,\ \frac{dn^{e}_{SRP}}{de} + \frac{1}{v_e}\frac{\partial v_e}{\partial e} n^{e}_{SRP} = 0 \tag{35}$$

The first characteristic can be obtained from Eq. (29) as

$$\frac{\sqrt{1-\hat{e}^2\sin^2\phi} + \hat{e}\cos\phi}{\sqrt{1-\hat{e}^2\sin^2\phi}} d\phi = \dot{\bar{\phi}} dt \tag{36}$$

which can be integrated as

$$\int \left(1 + \frac{\bar{e}\cos\phi}{\sqrt{1-\bar{e}^2\sin^2\phi}}\right) d\phi - \int \dot{\bar{\phi}} dt = C_\phi(\phi, t) \tag{37}$$

Therefore, the first characteristic function can be solved from the integration above as

$$C_\phi(\phi, t) = \phi + \sin^{-1}(\hat{e}\sin\phi) - \dot{\bar{\phi}} t \tag{38}$$

Similarly, the second characteristic can be integrated from Eq. (30) as

$$\int \frac{e}{\sin\left(\cos^{-1}\left[\frac{1}{2\hat{e}}\left(\frac{e^2}{\bar{e}^2} - 1 - \hat{e}^2\right)\right]\right)} de + \int \dot{\bar{\phi}}\bar{e}^2\hat{e}\, dt = C_e(e, t) \tag{39}$$

which has a simple form as

$$C_e(e, t) = \sin^{-1}\left(\frac{e^2 - e_f^2 - \bar{e}^2}{2e_f\bar{e}}\right) + \dot{\bar{\phi}} t \tag{40}$$

Besides, from Eq. (35), the number density can then be obtained from the first and second characteristic functions respectively, as

$$n^{\phi}_{SRP}(\phi, t) = \frac{\Phi_\phi(C_\phi(\phi, t))}{v_\phi(\phi)},\ n^{e}_{SRP}(e, t) = \frac{\Phi_e(C_e(e, t))}{v_e(e)} \tag{41}$$

where Φ_e and Φ_ϕ are some arbitrary functions of the characteristic equations and will be determined from the initial data $n^{\phi}_{SRP}(\phi, 0)$ and $n^{e}_{SRP}(e, 0)$ at the initial time t=0.

Just as in McInnes [14] and McInnes and Colombo [2], the initial data condition is selected $n^{\phi}_{SRP}(\phi, 0) = 1$ or $n^{e}_{SRP}(e, 0) = 1$, chosen as an example to demonstrate the wave-like distribution of number density on a precessing elliptical orbit. Combining the initial data $n^{\phi}_{SRP}(\phi, 0) = 1$ and $n^{e}_{SRP}(e, 0) = 1$ and Eq. (41) yields the forms of Φ_e and Φ_ϕ as

$$\Phi_\phi(C_\phi(\phi, 0)) = v_\phi(\phi),\ \Phi_e(C_e(e, 0)) = v_e(e) \tag{42}$$

It should be noted that the initial data condition $n^{\phi}_{SRP}(\phi,0)=1$ is not equivalent to $n^{e}_{SRP}(e,0)=1$ because there are non-linear mapping functions between them, i.e., G_{SRP} and G^{-1}_{SRP}. Thus, a uniform initial distribution about ϕ will be mapped to a non-uniform initial distribution about *e*, given by

$$n^{e}_{SRP}(e,0)=\frac{dN}{de}=\frac{dN}{d\phi}\cdot\frac{d\phi}{de}=n^{\phi}_{SRP}(\phi,0)\cdot\frac{dG^{-1}_{SRP}(e)}{de}=\frac{dG^{-1}_{SRP}(e)}{de} \tag{43}$$

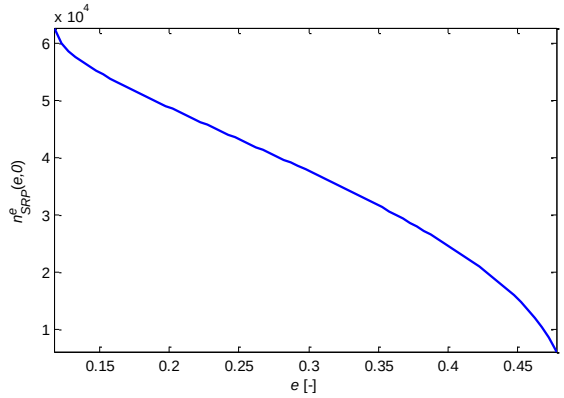

Fig.5 Non-uniform initial distribution of density about *e* derived from the uniform distribution about ϕ such that $n^{\phi}_{SRP}(\phi,0)=1$

and shown in Fig.5, where the area-to-mass ratio of the spacecraft is chosen as 10 m^2/kg, the mean eccentricity $\bar{e}$ is chosen as 0.3, and the semi-major axis of the elliptical orbit is chosen as 11,000km so that the frozen eccentricity is 0.1826. To determine the functional form of Φ_e and Φ_ϕ as functions of new variables z_1 and z_2, the inverse function of $z_1=C_{\phi}(\phi,0)$ is used to obtain ϕ as a function of z_1 as

$$\phi=\tan^{-1}\left(\frac{\sin z_1}{\hat{e}+\cos z_1}\right) \tag{44}$$

and the inverse function of $z_2=C_e(e,0)$ is used to obtain *e* as a function of z_2 as

$$e=\bar{e}\sqrt{1+\hat{e}^2+2\hat{e}\cos z_2} \tag{45}$$

Therefore, the arbitrary functions Φ_e and Φ_ϕ can be obtained from Eqs. (44) and (45) as

$$\Phi_{\phi}(z_1)=v_{\phi}\left(\tan^{-1}\frac{\sin z_1}{\hat{e}+\cos z_1}\right),\ \Phi_e(z_2)=v_e\left(\bar{e}\sqrt{1+\hat{e}^2+2\hat{e}\cos z_2}\right). \tag{46}$$

Now, combining Eqs. (29), (30), (38), (40), (41) and (46) yields the full closed-form solutions for the swarm number density with the initial data $n^{\phi}_{SRP}(\tilde{\phi},0)=1$ and $n^{e}_{SRP}(\tilde{e},0)=1$ as

$$n^{\phi}_{SRP}(\phi,t)=\frac{n^{\phi}_{SRP}(\tilde{\phi},0)\cdot v_{\phi}(\tilde{\phi})}{v_{\phi}(\phi)},\ n^{e}_{SRP}(e,t)=\frac{n^{e}_{SRP}(\tilde{e},0)\cdot v_e(\tilde{e})}{v_e(e)} \tag{47}$$

where $\tilde{\phi} = \tan^{-1}\dfrac{\sin C_\phi(\phi,t)}{\hat{e}+\cos C_\phi(\phi,t)}$ and $\tilde{e} = \bar{e}\sqrt{1+\hat{e}^2+2\hat{e}\cos C_e(e,t)}$. Thus, the full expressions of $n^{\phi}_{SRP}(\phi,t)$ and $n^{e}_{SRP}(e,t)$ are

$$n^{\phi}_{SRP}(\phi,t) = \frac{\sqrt{1-\bar{e}^2\sin^2\phi}+\hat{e}\cos\phi}{\sqrt{1-\bar{e}^2\sin^2\phi}} \cdot \frac{1+\hat{e}\cos\left[\phi+\sin^{-1}(\hat{e}\sin\phi)-\dot{\bar{\phi}}t\right]}{1+\hat{e}^2+2\hat{e}\cos\left[\phi+\sin^{-1}(\hat{e}\sin\phi)-\dot{\bar{\phi}}t\right]} \tag{48a}$$

$$n^{e}_{SRP}(e,t) = \frac{e\sin\left\{\cos^{-1}\left(\sin\left[\sin^{-1}\left(\dfrac{e^2-e_f^2-\bar{e}^2}{2e_f\bar{e}}\right)+\dot{\bar{\phi}}t\right]\right)\right\}}{\bar{e}\sqrt{1+\hat{e}^2+2\hat{e}\sin\left[\sin^{-1}\left(\dfrac{e^2-e_f^2-\bar{e}^2}{2e_f\bar{e}}\right)+\dot{\bar{\phi}}t\right]}\sin\left(\cos^{-1}\left[\dfrac{1}{2\hat{e}}\left(\dfrac{e^2}{\bar{e}^2}-1-\hat{e}^2\right)\right]\right)} \tag{48b}$$

The typical distributions of $n^{\phi}_{SRP}(\phi,t)$ are shown in Fig.6 with the initial condition $n^{\phi}_{SRP}(\phi,0)=1$, and $n^{e}_{SRP}(e,t)$ shown in Fig.7 with the initial condition $n^{e}_{SRP}(e,0)=1$, where the area-to-mass ratio of spacecraft is chosen as 10 m^2/kg and the semi-major axis of the elliptical orbit is chosen as 11,000km. For illustration, for the $\bar{e} > e_f$ case, the uniform initial density distribution on the ϕ-Θ space is forced by the velocity of ϕ to create a dense region centred on (ϕ_0,π), where ϕ_0 is the frozen pericentre angle and Θ is defined as $\Theta = \Theta_0 + \dot{\bar{\phi}}t$ (discussed later); for the $\bar{e} < e_f$ case, the actual value of $\phi = \tan^{-1}\frac{\bar{e}\sin\bar{\phi}}{e_f+\bar{e}\cos\bar{\phi}}$, $\bar{\phi}\in[0,2\pi]$ has a minimum value of $-\sin^{-1}\frac{\bar{e}}{e_f}$ and a maximum value of $+\sin^{-1}\frac{\bar{e}}{e_f}$, and the actual eccentricity has a minimum value of $e_f-\bar{e}$ and a maximum value of $e_f+\bar{e}$. These limits are used in Figs. 6 and 7. Except for the case presented in Fig.6a, any of the other three cases in Figs. 6 and 7 have two zero-density lines, and also infinite density at the boundaries of variables. An illustration of the physical scenarios using 50 single devices is shown in Fig.8 to demonstrate the evolution of number density from the initial condition $n^{\phi}_{SRP}(\phi,0)=1$ using the same parameters as Fig.6. It can be seen that the devices periodically gather or scatter in ϕ-e space corresponding to complex behaviour of the entire ensemble of devices. Similar evolution can also be seen for $n^{e}_{SRP}(e,0)=1$.

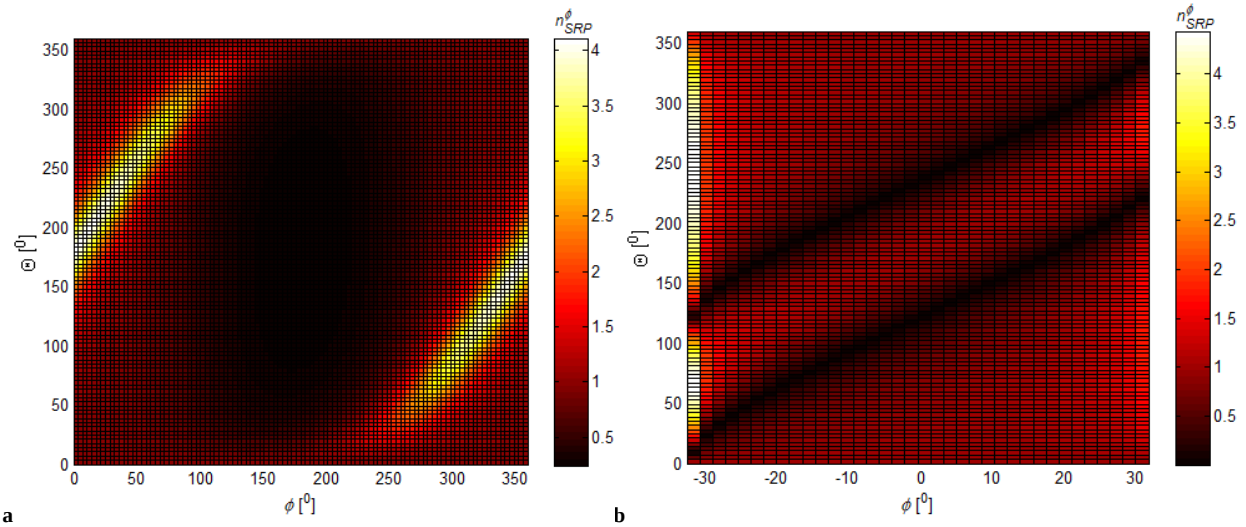

Fig.6 The distribution of number density on ϕ-Θ space: a the mean eccentricity $\bar{e}$ is chosen as 0.3, and ϕ ranges from 0^0 to 360^0; **b** the mean eccentricity $\bar{e}$ is chosen as 0.1, and ϕ ranges from $-32.9^0+\sigma$ to $32.9^0-\sigma$; where σ is chosen as 0.03^0 to avoid the numerical singularity.

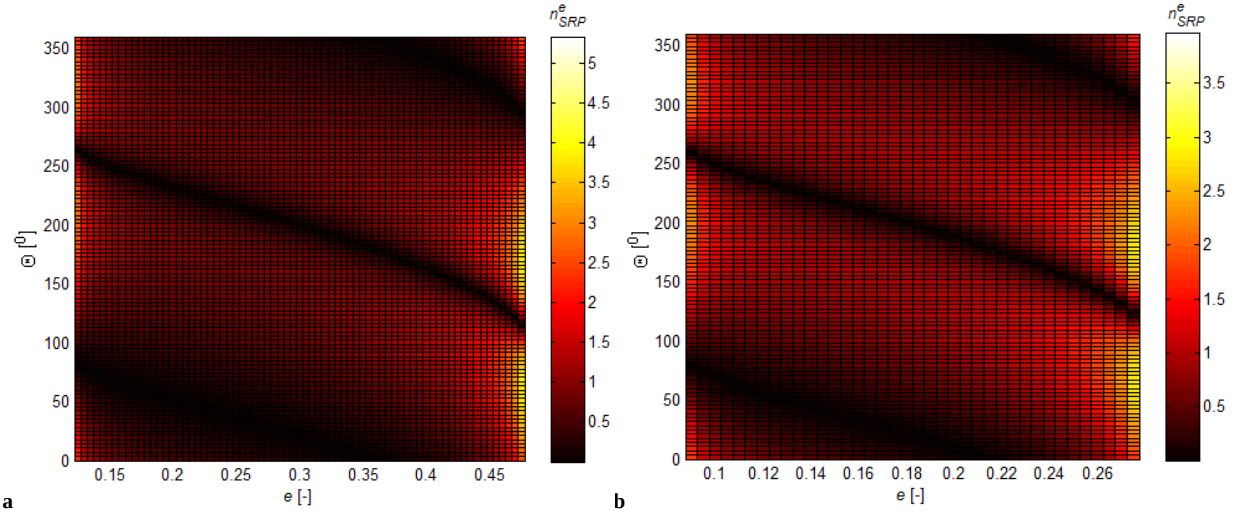

Fig.7 The distribution of number density on *e*-Θ space: a the mean eccentricity $\bar{e}$ is chosen as 0.3, and *e* ranges from $0.1174+\sigma$ to $0.4826-\sigma$; **b** the mean eccentricity $\bar{e}$ is chosen as 0.1, and *e* ranges from $0.0826+\sigma$ to $0.2826-\sigma$; where σ is chosen as 0.005 to avoid the numerical singularity.

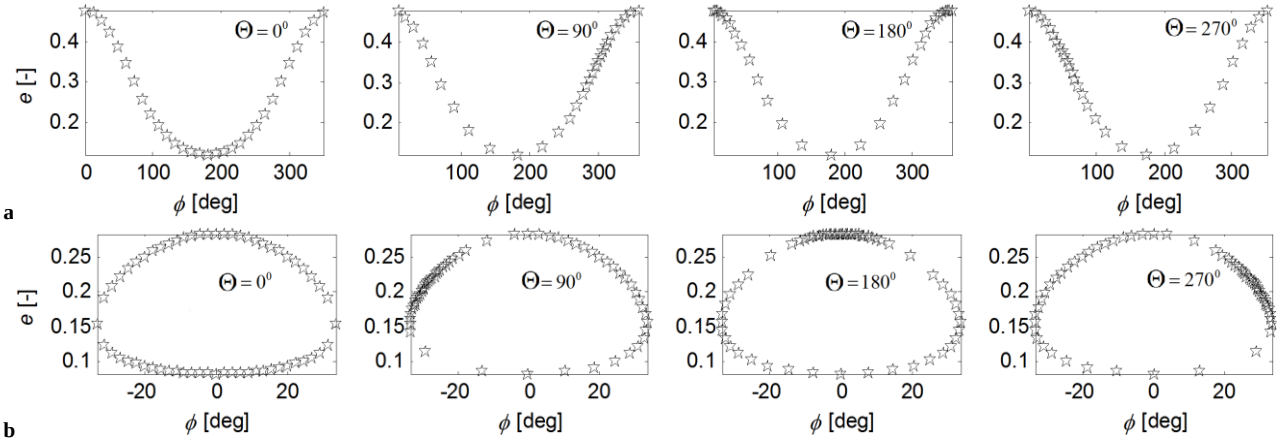

Fig.8 The evolution of number density displayed by 50 devices in ϕ-*e* space: a the mean eccentricity $\bar{e}$ is chosen as 0.3; **b** the mean eccentricity $\bar{e}$ is chosen as 0.1.

Some discussion of the small denominator and its limitations are now required for the closed-form solutions $n_{SRP}^{\phi}(\phi,t)$ and $n_{SRP}^{e}(e,t)$ as follows.

Firstly, the term $\dot{\bar{\phi}}t$ is periodic about 2π in the closed-form solution above, which can be seen by the periodic trigonometric functions in Eq. (45). Therefore, an angle variable $\Theta=\Theta_0+\dot{\bar{\phi}}t\in[0,2\pi]$ is introduced to replace the time term in all relevant equations for simplicity. Besides, the variable Θ is used to replace all the time terms $\dot{\bar{\omega}}t$ for the J_2 and J_3 precessing ellipse case in **Section III.B** as well.

Secondly, for a given spacecraft area-to-mass ratio and semi-major axis, the ranges of the variables ϕ and e depend on the value of the mean eccentricity $\bar{e}$ only, which is classified as

$$\begin{aligned} e &\in \left[\left|\bar{e}-e_f\right| \quad \bar{e}+e_f\right] \\ \phi &\in \begin{cases} [0 \quad 2\pi], & \bar{e}>e_f \\ \left[-\sin^{-1}\frac{\bar{e}}{e_f} \quad +\sin^{-1}\frac{\bar{e}}{e_f}\right], & \bar{e}\le e_f \end{cases} \end{aligned} . \tag{49}$$

For the case $\bar{e}=e_f$, i.e., $\hat{e}=1$, the minimum of the actual eccentricity e is zero, which may cause a small denominator in Eq. (30). Thus, the density distribution at $e=0$ (ϕ is equal to $\pm\frac{\pi}{2}$ at this moment) can be found by the limit when $\bar{\phi}\to\pi$ as:

$$n_{SRP}^{e}(0,\Theta)=\lim_{\bar{\phi}\to\pi}\frac{v_e(\tilde{e})}{v_e(e)}=\frac{\dot{\bar{\phi}}\bar{e}\cos\frac{\Theta}{2}}{\dot{\bar{\phi}}\bar{e}}=\cos\frac{\Theta}{2},\ \Theta\in[-\pi,+\pi]. \tag{50}$$

Thirdly, substituting $\tilde{\phi}=\tan^{-1}\dfrac{\sin C_\phi(\phi,t)}{\hat{e}+\cos C_\phi(\phi,t)}$ and $\tilde{e}=\bar{e}\sqrt{1+\hat{e}^2+2\hat{e}\cos C_e(e,t)}$ into Eqs. (29) and (30) respectively yields $v_\phi(\tilde{\phi})=\dot{\bar{\phi}}\dfrac{\left|1+\hat{e}\cos C_\phi(\phi,\Theta)\right|}{\left|1+\hat{e}\cos C_\phi\right|+\hat{e}\cos C_\phi}$ and $v_e(\tilde{e})=-\dfrac{\dot{\bar{\phi}}\bar{e}^2\hat{e}}{e}\sin C_e(e,\Theta)$, which are the numerators of the closed-form solutions in Eqs. (48a) and (48b). It is interesting to note that for the case $\bar{e}>e_f$ there are two conditions $\hat{\Theta}_1^{\phi}$ (or $\hat{\Theta}_1^{e}$) and $\hat{\Theta}_2^{\phi}$ (or $\hat{\Theta}_2^{e}$), defined as the zero-density lines, such that

$$\hat{\Theta}_{1,2}^{\phi}=\pm\cos^{-1}\left(-\frac{1}{\hat{e}}\right)-\phi-\sin^{-1}(\hat{e}\sin\phi),\ \hat{\Theta}_{1,2}^{e}=0(\pi)-\sin^{-1}\left(\frac{e^2-e_f^2-\bar{e}^2}{2e_f\bar{e}}\right) \tag{51}$$

which will make $v_e(\tilde{e})$ equal to zero, and then make $n(\phi,e,\hat{\Theta})$ equal to zero, which are also verified by the two zero-density lines in Figs. 6 and 7.

Fourthly, for the case $\bar{e} > e_f$, both the minimum and maximum of ϕ and e will make the denominator functions of $v_e(e)$ and $v_\phi(\phi)$ equal to zero, which means that the density tends to infinity all the times except the specified conditions $\Theta=2k\pi$, $k=1,2,3,\ldots$, making the density equal to 1. From the physical viewpoint, the swarm of devices are forced by the laws formulated by $v_e(e)$ and $v_\phi(\phi)$ away from the uniform initial distribution; however, the null-velocity states of $v_e(e)=0$ and $v_\phi(\phi)=0$ result in a larger density than other states. The same conclusion can be achieved for the density $n^e_{SRP}(e,t)$ even for the case $\bar{e} < e_f$. Actually, an infinite density is in principle acceptable because it does not change the total number $N(t)=\int_{\phi_{\min}}^{\phi_{\max}} n^\phi_{SRP}(\phi)d\phi$ of swarm devices, whose rate with respect to time is simplified by Eq. (31) as

$$\dot{N}(t)=\frac{d}{dt}\int_{\phi_{\min}}^{\phi_{\max}} n^\phi_{SRP}(\phi)d\phi=\int_{\phi_{\min}}^{\phi_{\max}}\frac{\partial n^\phi_{SRP}}{\partial t}d\phi=-\int_{\phi_{\min}}^{\phi_{\max}}\frac{\partial\left(v_\phi n^\phi_{SRP}\right)}{\partial t}nd\phi=-v_\phi n^\phi_{SRP}\Big|_{\phi_{\min}}^{\phi_{\max}}=-v_\phi\left[\tilde{\phi}(\phi)\right]_{\phi_{\min}}^{\phi_{\max}} \tag{52}$$

where $\tilde{\phi}=\arctan\frac{\sin C_\phi(\phi,t)}{\hat{e}+\cos C_\phi(\phi,t)}$. The numerical implementation later indicates that $v_\phi\left[\tilde{\phi}(\phi_{\min})\right]=v_\phi\left[\tilde{\phi}(\phi_{\max})\right]$ for all the time t, which means $\dot{N}(t)=0$. Obviously, the total number of devices is invariant for the case $\bar{e} > e_f$ as well, which is equal to $N(t)=N(0)=\oint n^\phi_{SRP}(\phi,0)d\phi=\oint 1\cdot d\phi=2\pi$.

According to the statements above, the uniform initial data distribution about ϕ for the case $\bar{e} > e_f$ does not result in infinite density at $[0, 2\pi]$ because the velocity v_ϕ of ϕ at the conditions $\phi=0$ and $\phi=\pi$ are non-zero, so that the finite density distribution about e can be derived from the mapping $e=G_{SRP}(\phi)$, as shown in Fig.9 by the same parameters as Fig.6. Compared with the infinite density caused by the uniform initial distribution, the finite density about e is created by the non-uniform initial distribution demonstrated in Fig.5, because the numerator $n^e_{SRP}(\tilde{e})$ in Eq. (48b) is no longer equal to 1, and has a finite limit of $\lim_{e\to e_{\min}(e_{\max})}=\frac{n^e_{SRP}(\tilde{e},0)}{v_e(e)}$ when e approaches its boundaries.

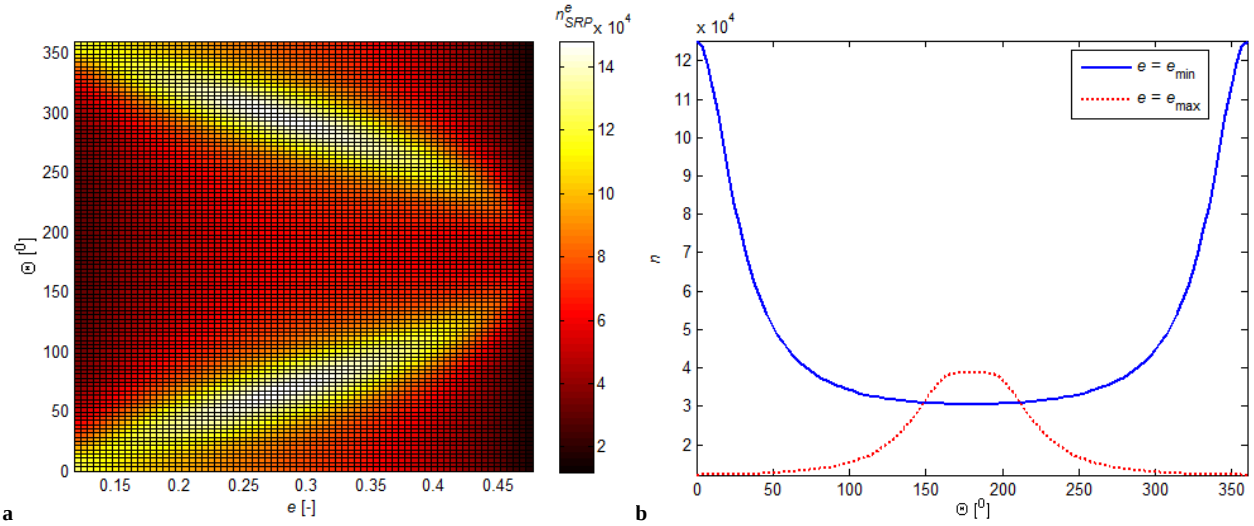

a **b**

Fig.9 Distribution of number density on *e*-Θ space created by a non-uniform initial distribution: the initial data condition is non-uniform as addressed in Eq. (42); **a** the 2-D distribution on *e*-Θ space**; b** the time history of density on the boundaries.

B. Continuity Equation Modelled for J_2 and J_3 Perturbations

Similar to elliptical orbits perturbed by J_2 and SRP, the continuum evolution for the J_2 and J_3 case is written by the argument of perigee ω as

$$\frac{\partial n^e_{J_3}}{\partial t} + v_e \frac{\partial n^e_{J_3}}{\partial e} + \frac{\partial v_e}{\partial e} n^e_{J_3} = 0 \cdot \tag{53a}$$

$$\frac{\partial n^\omega_{J_3}}{\partial t} + v_\omega \frac{\partial n^\omega_{J_3}}{\partial \omega} + \frac{\partial v_\omega}{\partial \omega} n^\omega_{J_3} = 0 \cdot \tag{53b}$$

with the characteristic functions derived from Eqs. (10) and (11) as

$$D_\omega(\omega,t) = \omega - \sin^{-1}(\hat{e}\cos\omega) - \dot{\bar{\omega}}t \tag{54}$$

$$D_e(e,t) = \sin^{-1}\left(\frac{e^2 - e_f^2 - \bar{e}^2}{2e_f\bar{e}}\right) - \dot{\bar{\omega}}t \tag{55}$$

Based on the derivations in **Section III.A**, the number density can then be obtained as

$$n^\omega_{J_3}(\omega,t) = \frac{\Psi_\omega(D_\omega(\omega,t))}{v_\omega(\omega)},\ n^e_{J_3}(e,t) = \frac{\Psi_e(D_e(e,t))}{v_e(e)} \tag{56}$$

where Ψ_e and Ψ_ω are some arbitrary functions of the characteristic equation and will be determined from the initial data $n^\omega_{J_3}(\omega,0)$ and $n^e_{J_3}(e,0)$ at the initial time t=0.

Combining the uniform initial data distribution and Eq. (56) yields the arbitrary functions Ψ_e and Ψ_ω formulated by new variables $y_1 = D_\omega(\omega,0)$ and $y_2 = D_e(e,0)$ as

$$\Psi_{\omega}(y_1)=v_{\omega}\left(\tan^{-1}\frac{\hat{e}+\sin y_1}{\cos y_1}\right),\ \Psi_e(y_2)=v_e\left(\bar{e}\sqrt{1+\hat{e}^2+2\hat{e}\sin y_2}\right). \tag{57}$$

Now combining Eqs. (10), (11), (54), (55), (56) and (57) yields the full closed-form solution for the number density with the uniform initial data distribution as

$$n^{\omega}_{J_3}(\omega,t)=\frac{\sqrt{1-\hat{e}^2\cos^2\omega}+\hat{e}\sin\omega}{\sqrt{1-\bar{e}^2\cos^2\omega}}\cdot\frac{1+\hat{e}\sin\left[\omega-\sin^{-1}(\hat{e}\cos\omega)-\dot{\bar{\omega}}t\right]}{1+\hat{e}^2+2\hat{e}\sin\left[\omega-\sin^{-1}(\hat{e}\cos\omega)-\dot{\bar{\omega}}t\right]} \tag{58a}$$

$$n^{e}_{J_3}(e,t)=\frac{e\cos\left[\sin^{-1}\left(\dfrac{e^2-e_f^2-\bar{e}^2}{2e_f\bar{e}}\right)-\dot{\bar{\omega}}t\right]}{\bar{e}\sqrt{1+\hat{e}^2+2\hat{e}\sin\left[\sin^{-1}\left(\dfrac{e^2-e_f^2-\bar{e}^2}{2e_f\bar{e}}\right)-\dot{\bar{\omega}}t\right]\cos\left(\sin^{-1}\left[\dfrac{1}{2\hat{e}}\left(\dfrac{e^2}{\bar{e}^2}-1-\hat{e}^2\right)\right]\right)}} \tag{58b}$$

The typical distributions of $n^{\omega}_{J_3}(\omega,t)$ are shown in Fig.10 with the initial condition $n^{\omega}_{J_3}(\omega,0)=1$, and $n^{e}_{J_3}(e,t)$ shown in Fig.11 with the initial condition $n^{e}_{J_3}(e,0)=1$, where the area-to-mass ratio of spacecraft is chosen as 10 m^2/kg and the semi-major axis of the given elliptical orbit is chosen as 11,000km. For the $\bar{e}>e_f$ case, the uniform initial density distribution on the ω-Θ space is forced by the velocity of ω to create a dense region centred on (ω_0,π), where ω_0 is the frozen argument of perigee; for the $\bar{e}<e_f$ case, the actual value of $\omega=\tan^{-1}\frac{\bar{e}\sin\bar{\omega}+e_f}{\bar{e}\cos\bar{\omega}}$, $\bar{\omega}\in[0,2\pi]$, has a minimum value of $\frac{\pi}{2}-\sin^{-1}\frac{\bar{e}}{e_f}$, and a maximum value of $\frac{\pi}{2}+\sin^{-1}\frac{\bar{e}}{e_f}$ and the actual eccentricity has a minimum value of $e_f-\bar{e}$ and a maximum value of $e_f+\bar{e}$. These limits are used in Figs. 10 and 11. For comparison with Figs. 6 and 7, the frozen eccentricity is chosen as the same value of 0.1826, although this frozen eccentricity cannot be reached by the J_2 and J_3 perturbations. Compared with Figs. 6 and 7, the transition of frozen eccentricity from (e_f, 0) to (0, e_f) causes the distribution of density on the $\phi(\omega)$-Θ space to shift 90^0 along the $\phi(\omega)$ direction but has no change along the Θ direction. The change in the shape of the distributions on the e-Θ space can be seen from the zero-density lines, i.e., $\sin C_e(e,\Theta)=0$ for J_2 and SRP perturbations and $\cos D_e(e,\Theta)=0$ for J_2 and J_3 perturbations so that the transition causes the two distributions to have mirror symmetry about the $\Theta-\frac{3}{4}\pi=0$ line. The evolution of the number density of devices from the initial condition $n^{\omega}_{J_3}(\omega,0)=1$, with the same parameters as Fig.10, is shown in Fig. 12 with 50 single devices periodically gathering or scattering on ω-e space. Similar evolution can also be seen for $n^{e}_{J_3}(e,0)=1$.

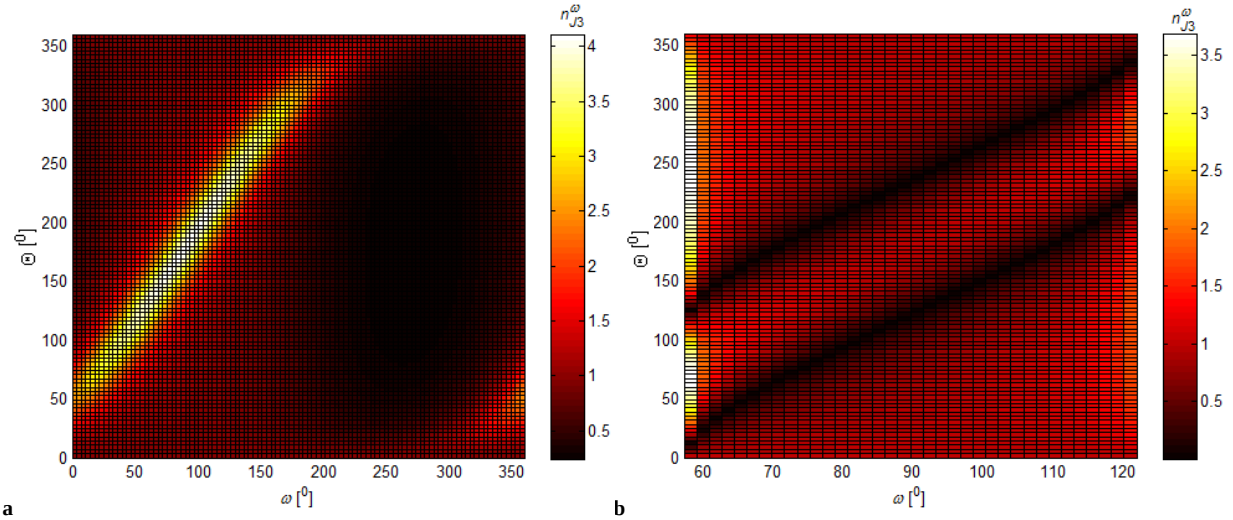

Fig.10 The distribution of number density on ω-Θ space: a the mean eccentricity $\bar{e}$ is chosen as 0.3, and ϕ ranges from 0^0 to 360^0; **b** the mean eccentricity $\bar{e}$ is chosen as 0.1, and ϕ ranges from $56.79^0+\sigma$ to $123.21^0-\sigma$; where σ is chosen as 0.03^0 to avoid the numerical singularity.

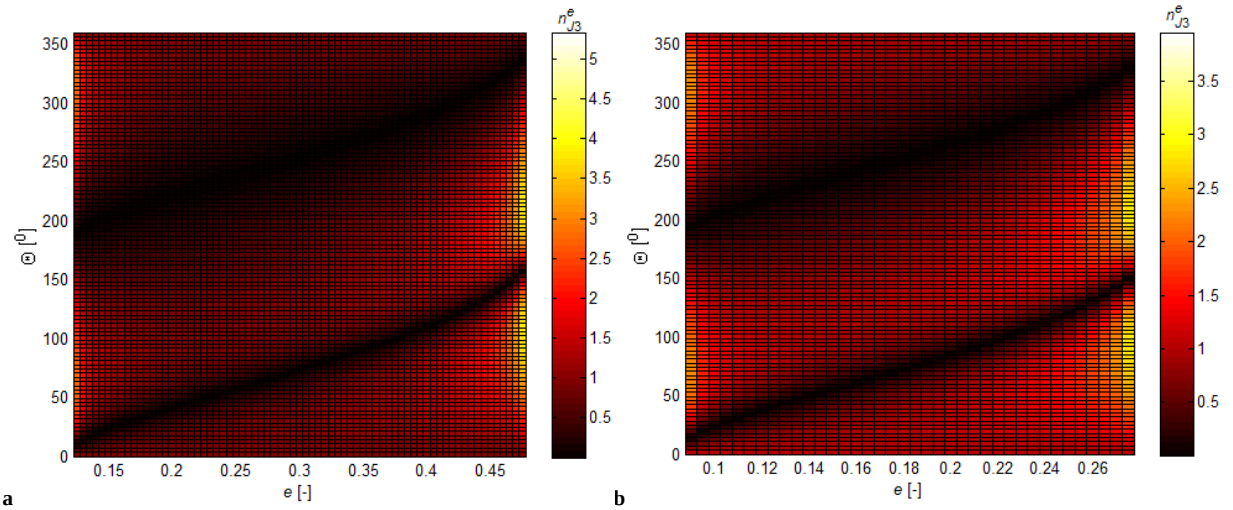

Fig.11 The distribution of number density on *e*-Θ space: a the mean eccentricity $\bar{e}$ is chosen as 0.3, and e ranges from $0.1174+\sigma$ to $0.4826-\sigma$; **b** the mean eccentricity $\bar{e}$ is chosen as 0.1, and e ranges from $0.0826+\sigma$ to $0.2826-\sigma$; where σ is chosen as 0.005 to avoid the numerical singularity.

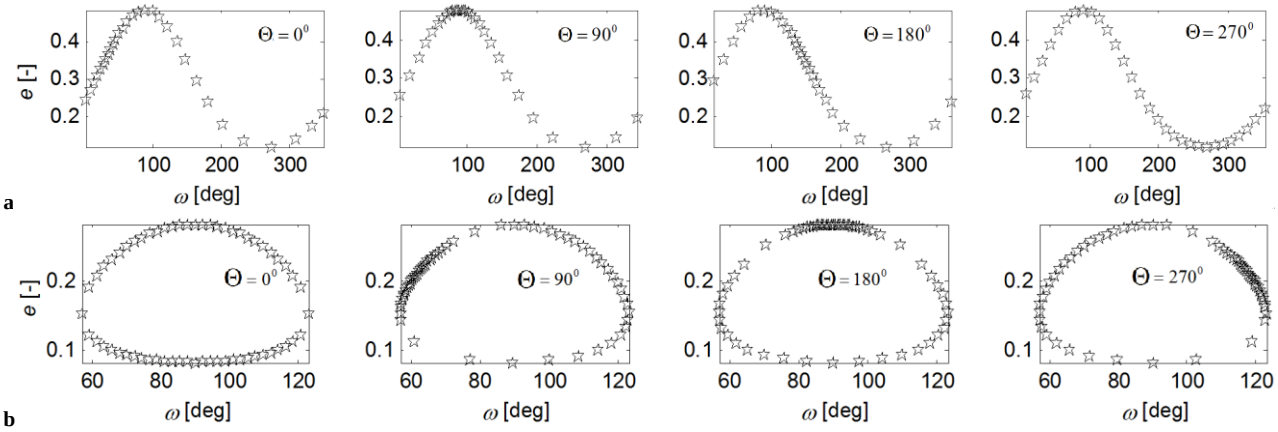

Fig.12 Evolution of number density displayed by 50 single devices on ω-e space: a the mean eccentricity $\bar{e}$ is chosen as 0.3; **b** the mean eccentricity $\bar{e}$ is chosen as 0.1.

C. Comparison between Analytic and Numerical Number Density Evolutions

Taking the J_2-SRP problem for example, the full dynamics defined by Eqs. (13) are propagated by a Runge-Kutta 7(8) integrator from the initial eccentricity $e_0 = e_f + \bar{e}$ and ϕ_0=0^0 to yield a one-period evolution of (e,ϕ). Then, several points are chosen with a uniform distribution about ϕ from the (e,ϕ) evolution as new initial conditions to propagate the full dynamics in parallel. The swarm number $N(\phi,\Theta)$ in the any interval $\phi\times\Theta\in\left[\phi-\frac{1}{2}\Delta\phi \quad \phi+\frac{1}{2}\Delta\phi\right]\times\left[\Theta-\frac{1}{2}\Delta\Theta \quad \Theta+\frac{1}{2}\Delta\Theta\right]$ is obtained statistically, where the interval step $\Delta\Theta$ and $\Delta\phi$ are chosen as 1^0 and 1^0, respectively. The numerical density is approximated as $n'(\phi,\Theta)=N(\phi,\Theta)/\Delta\phi$.

Thus, the comparison is made by the relative errors of the analytic results $n(\phi,\Theta)$ and the numerical results $n'(\phi,\Theta)$, which is defined as

$$\varepsilon=\left|\frac{n(\phi,\Theta)-n'(\phi,\Theta)}{n'_{\max}}\right| \tag{59}$$

where the denominator $n'_{\max}$ is the maximum of the numerical results, instead of $n'(\phi,\Theta)$ to avoid the singular case at the zero-density lines $n(\phi,\Theta)=0$ when $\bar{e}<e_f$. Besides, to avoid the infinite case at $\phi_{\min}$ or $\phi_{\max}$ when $\bar{e}<e_f$, the comparison is made within the subinterval $\phi\in\left[-\frac{1}{2}\phi_{\min} \quad \frac{1}{2}\phi_{\max}\right]$, which is shown in Fig.13. Compared with the analytic distribution of number density on the ϕ-Θ space in Fig.6, it is concluded from Fig.13 that the relative error reaches its maximum at the peak of the analytic distribution for the $\bar{e}>e_f$ case, and reaches its maximum at the zero-density lines of the analytic distribution for the $\bar{e}<e_f$ case.

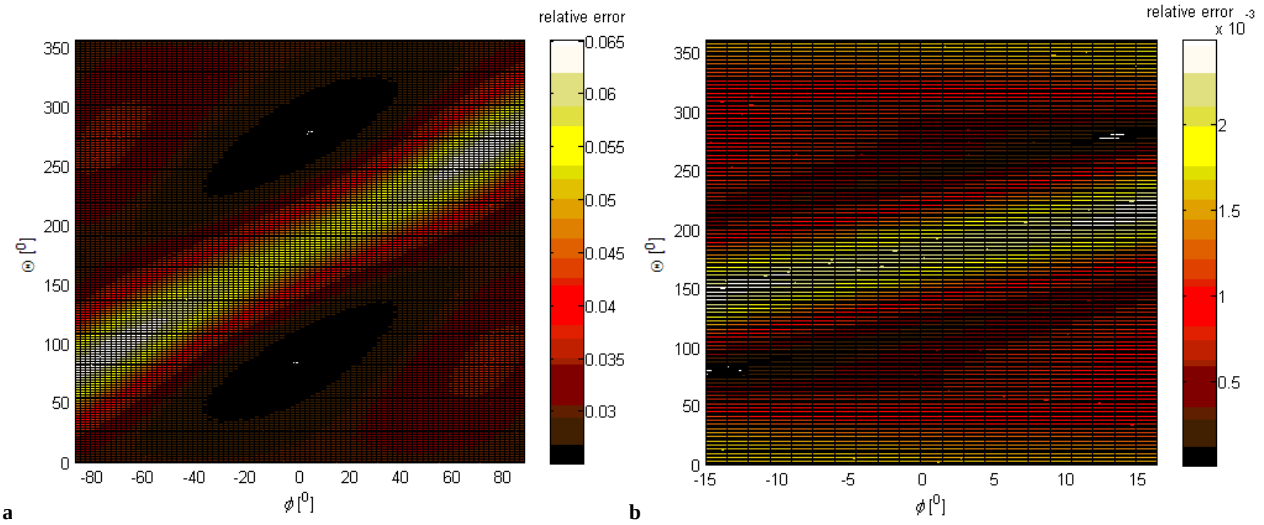

a b

Fig.13 Relative error of analytic number density solution to the numerical number density: a=11,000km and A/m= 10m^2/kg; **a** $\bar{e}=0.3$; **b** $\bar{e}=0.1$.

Due to the analytic density derived from the linearized dynamics, it is necessary to investigate the relationship between the mean eccentricity and relative errors, which are shown in Fig.14 for the J_2-J_3 and J_2-SRP problems, respectively. It is shown that the analytic number density solution has increasing errors with increasing mean eccentricity, but has a modest error of less than 12% even for a large $\bar{e}=0.3$.

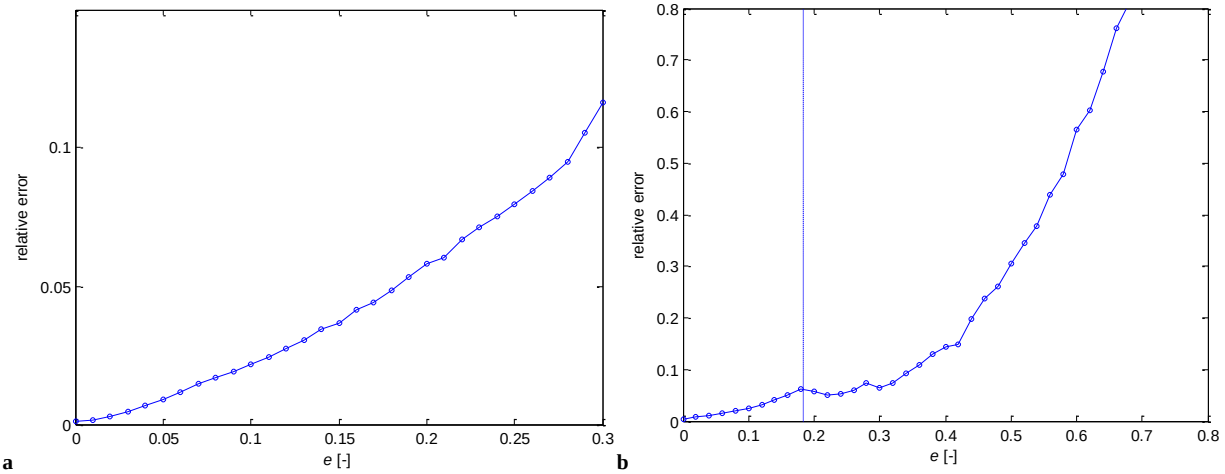

a b

Fig.14 Relationship between the mean eccentricity and the relative error of the analytic number density solution: **a** J_2-J_3 problem: a=7178.137km and i=108^0; **b** planar J_2-SRP problem: a=11,000km and A/m= 10m^2/kg.

Moreover, different numbers of swarm members can be employed to investigate the relationship between the relative errors and the number of swarm members, shown in Fig.15. It is interesting to note that a larger number of swarm members may cause less error, but the error will decrease until the employed number is approximately 3600. Thus, for all scenarios used in this paper, the minimum number of swarm members can be set as 3600. However, only 50 devices

are used for the purpose of displaying the evolution of the swarm number density in Figs. 8 and 12, since too many devices will make the figures filled with points and unclear.

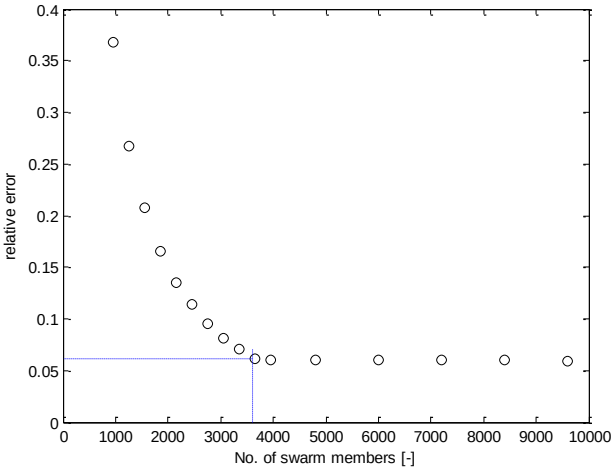

Fig.15 Relationship between the number of swarm members and the relative error of the analytic number density solution: a=11,000km and A/m= 10m^2/kg, $\bar{e} = 0.3$.

IV. Applications of Continuum Density Models

A. *Number of Swarm Devices with Distant Apogees for J_2 and SRP Perturbations*

The closed-form solution has potential application in predicting the time-dependent number of swarm devices which have apogees further than some critical radius r_a^{crital}, for example for the purpose of measuring the deep magnetic tail. This can be found from

$$N(t) = \int_{\Pi} n_{SRP}^{\phi}(\phi, t) d\phi \tag{60}$$

where the area Π is a range of $[e_1, e_2]$ derived from $r_a^{crital} \le a(1+e) \le r_a^{\max}$ for the given invariant semi-major axis a and the maximum radius of apogee $r_a^{\max}$ (for example restricted by the communications link budget), i.e., $e_1 = \frac{r_a^{crital}}{a} - 1$ and $e_2 = \frac{r_a^{\max}}{a} - 1$, shown in Fig.16.

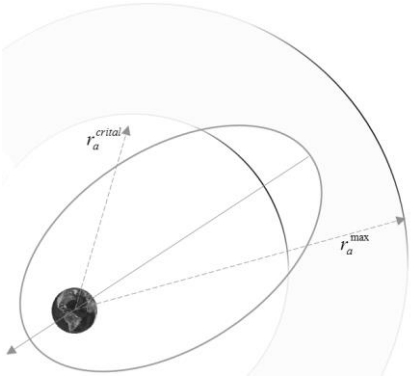

Fig.16 The geometry of required apogee between $r_a^{\max}$ and r_a^{crital}.

To proceed, integrating Eq. (60) with the variable ϕ, it is necessary to derive the inverse function of G_{SRP}^{-1} mapping from e to ϕ for the given e_f and $\bar{e}$. Due to the symmetric geometry presented in Fig.2, two intervals labelled as I and II with two pairs of lower and upper values of ϕ can be solved as $\phi_{lower}^1 = G_{SRP}^{-1}(e_1)$ and $\phi_{upper}^1 = G_{SRP}^{-1}(e_2)$ for Interval I, $\phi_{lower}^2 = -G_{SRP}^{-1}(e_2)$ and $\phi_{upper}^2 = -G_{SRP}^{-1}(e_1)$ for Interval II. Thus, the integration of the swarm to obtain the total number of devices within the apogee limits can be written as

$$N_i(t) = \int_{\phi_{lower}^i}^{\phi_{upper}^i} n_{SRP}^{\phi}(\phi,t)d\phi,\ i=1,2. \tag{61}$$

where $N_1(t)$ is the integration in Interval I, and $N_2(t)$ in Interval II. Differentiating Eq. (39) with respect to the variable ϕ yields

$$1+\frac{\hat{e}\cos\phi}{\sqrt{1-\hat{e}^2\sin^2\phi}} = \frac{\partial C_\phi(\phi,t)}{\partial\phi} \tag{62}$$

and then substituting Eqs. (39) and (61) into Eq. (49a) yields

$$N_i(t) = \int_{lower}^{\phi_{\text{upper}}} \frac{\partial C_\phi(\phi,t)}{\partial\phi}\cdot\frac{1+\hat{e}\cos\left[C_\phi(\phi,t)\right]}{1+\hat{e}^2+2\hat{e}\cos\left[C_\phi(\phi,t)\right]}d\phi \tag{63}$$

Therefore, replacing the variable ϕ in Eq. (63) by $C_\phi(\phi,t)$ provides

$$N_i(t) = \int_{C_{\text{lower}}}^{C_{upper}} \frac{1+\hat{e}\cos C}{1+\hat{e}^2+2\hat{e}\cos C}dC \tag{64}$$

which can be simplified as

$$N_i = \frac{1}{2}\left[C+2\frac{1-\hat{e}}{1+\hat{e}}\tan^{-1}\left(\frac{1-\hat{e}}{1+\hat{e}}\tan\frac{C}{2}\right)\right]_{C_{lower}}^{C_{upper}}. \tag{65}$$

Therefore, the closed-form of the integration can be derived from Eqs. (39) and (65) as

$$N_i(t)=\frac{1}{2}\left(\phi^i_{upper}-\phi^i_{lower}\right)+\frac{1}{2}\left[\sin^{-1}\left(\hat{e}\sin\phi^i_{upper}\right)-\sin^{-1}\left(\hat{e}\sin\phi^i_{lower}\right)\right]$$
$$+\frac{1}{2}\frac{1-\hat{e}}{1+\hat{e}}\left[\tan^{-1}\left(\frac{1-\hat{e}}{1+\hat{e}}\tan\frac{\phi^i_{upper}+\sin^{-1}\left(\hat{e}\sin\phi^i_{upper}\right)-\dot{\bar{\omega}}t}{2}\right)-\tan^{-1}\left(\frac{1-\hat{e}}{1+\hat{e}}\tan\frac{\phi^i_{lower}+\sin^{-1}\left(\hat{e}\sin\phi^i_{lower}\right)-\dot{\bar{\omega}}t}{2}\right)\right], \quad i=1,2 \tag{66}$$

For a practical mission exploring the deep magnetic tail, the allowed eccentricities are assumed to belong to the set $[\kappa_1, \kappa_2]$, where $\kappa=\frac{e-e_{\min}}{e_{\max}-e_{\min}}$, and the time history of the fraction of the accessible devices (relative to the total number, i.e., 2π) is illustrated in Fig.17 using the same parameters as Fig.10. It can be seen that the swarm can achieve spatially dense measurements near $\Theta=90^0$ and 270^0.

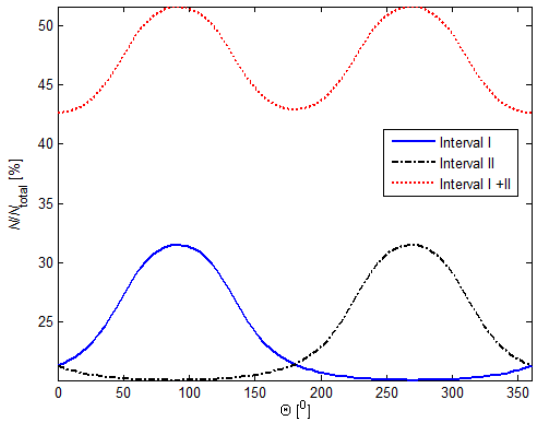

Fig.17 The time history of the fraction of accessible devices relative to the total number: the initial data condition is uniform as $n^{\phi}_{SRP}(\phi,0)=1$ and κ_1 and κ_2 are chosen as 0.3 and 0.9 respectively.

B. Number of Satellites Visible Above the Horizon for the J_2 and J_3 Perturbations

As another illustration, the closed-form solution for the J_2 and J_3 perturbations will be used to predict the number of swarm members with apogees less than a critical radius r_a^{crital}, for example to obtain the high resolution images, as shown in Fig.18. The number of devices is then given by

$$N(t)=\int_{\Pi} n^{\omega}_{J_3}(\omega,t)d\omega \tag{67}$$

where the area Π corresponds to a range of $[e_{\max}, e_c]$ derived from $e_c=\frac{r_a^{crital}}{a}-1$ for the given invariant semi-major axis a.

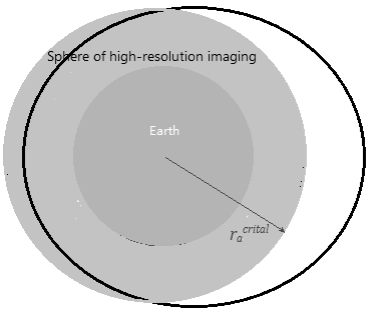

Fig.18 Sphere of high-resolution imaging for orbit apogee less than r_a^{crital}.

The inverse function of $F_{J_3}^{-1}$ is employed to yield the lower and upper value of ω for the integration above, as $\omega_{lower} = F_{J_3}^{-1}(e_c)$ and $\omega_{upper} = \pi - F_{J_3}^{-1}(e_c)$. Similar to the derivations in **Section IV.A**, the number integration of swarm members less than a critical apogee radius can be found from the characteristic function as

$$N(t) = \int_{D_{lower}}^{D_{upper}} \frac{1+\hat{e}\sin D_\omega}{1+\hat{e}^2+2\hat{e}\sin D_\omega} dD_\omega \tag{68}$$

which can be simplified as

$$N = \frac{1}{2}\left[D_\omega - 2\tan^{-1}\left(\frac{\hat{e}^2+1}{\hat{e}^2-1}\tan\frac{D_\omega}{2} + \frac{2\hat{e}}{\hat{e}^2-1} \right) \right]_{D_{lower}}^{D_{upper}}. \tag{69}$$

Therefore, the closed-form of the integration can be derived from Eqs. (55) and (69) as

$$\begin{aligned} N(t) = {} & \frac{1}{2}\left(\omega_{upper} - \omega_{lower}\right) - \frac{1}{2}\left[\sin^{-1}\left(\hat{e}\cos\omega_{upper}\right) - \sin^{-1}\left(\hat{e}co\omega_{lower}\right)\right] \\ & + 2\left[\tan^{-1}\left(\frac{\hat{e}^2+1}{\hat{e}^2-1}\tan\frac{\omega_{upper} - \sin^{-1}\left(\hat{e}\cos\omega_{upper}\right) - \dot{\bar{\omega}}t}{2} + \frac{2\hat{e}}{\hat{e}^2-1} \right) - \tan^{-1}\left(\frac{\hat{e}^2+1}{\hat{e}^2-1}\tan\frac{\omega_{lower} - \sin^{-1}\left(\hat{e}\cos\omega_{lower}\right) - \dot{\bar{\omega}}t}{2} + \frac{2\hat{e}}{\hat{e}^2-1} \right) \right] \end{aligned} \tag{70}$$

For a practical imaging mission, an eccentricity less than e_c is now required and the time history of the fraction of the number of devices relative to the total number $N(t) = N(0) = \int_{\omega_{\min}}^{\omega_{\max}} n_{J_3}^{\omega}(\omega,0)d\omega = \int_{\omega_{\min}}^{\omega_{\max}} 1\cdot d\omega = \omega_{\max} - \omega_{\min}$, is illustrated in Fig.19, where the mean semi-major axis is chosen to be 7178.137km, the mean inclination is 108^0 so that the frozen eccentricity is 0.001, and the mean eccentricity $\bar{e}$ is chosen as 0.8, and e_c is chosen as 0.4. The swarm can achieve the dense measurements near $\Theta=180^0$.

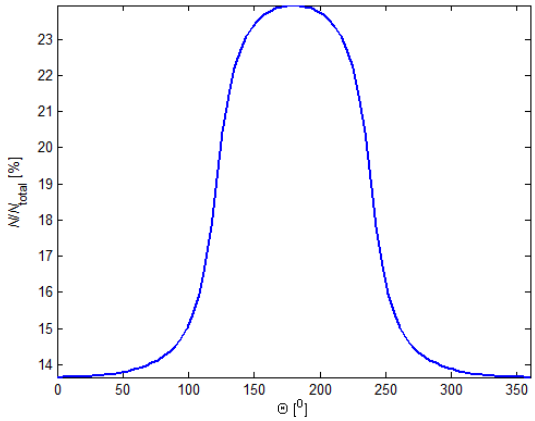

Fig.19 The time history of the percent of devices relative to the total number: the initial data condition is uniform as $n^{\omega}_{J_3}(\omega,0)=1$.

V. Conclusion

Wave-like patterns have been presented using a continuum approach by deriving closed-form solutions to continuity partial differential equations (PDEs) for the number density of swarm devices. By removing the osculating orbital elements, only the long-period eccentricity and argument of perigee angle in the J_2 and solar radiation pressure (SRP) cases are used to investigate the natural evolution of such wave-like patterns. As a comparison, the transition of the frozen eccentricity in the J_2 and SRP perturbation case to the J_2 and J_3 perturbation case causes the distribution of density to shift 90^0 along the direction of argument of perigee angle, and causes the two distributions to have mirror symmetry about the eccentricity with each other. Zero-density lines in the density distribution are found, as well as infinite density at the boundaries of eccentricity. Comparison between the analytic and numerical number density evolution is made through the relative errors of the analytic results and the numerical results, which can be used to yield the range of applicable eccentricity based the maximum error tolerance, as well as the minimum number of swarm members required to approximate continuous evolution.

Moreover, the closed-form solutions have potential applications in predicting the fraction of high area-to-mass ratio swarm devices which have apogees further than a critical radius for the purpose of measuring the magnetic tail, as well as predicting the number of Earth-observing devices which require an apogees less than some critical radius for imaging.

Acknowledgments

Ming Xu acknowledges the support of the Fundamental Research Funds for the Central Universities and China Scholarship Council program (201506025138), and Colin McInnes acknowledges the support of a Royal Society Wolfson Research Merit Award.

References

[1] Wertz, J. R., "Coverage, Responsiveness and Accessibility for Various Responsive Orbits," 3rd Responsive Space Conference, April 25-28, 2005, Los Angeles, CA, AIAA Paper RS3-2005-2001.

[2] McInnes, C. R., Colombo, C., "Wave-like patterns in an elliptical satellite ring", *Journal of Guidance, Control, and Dynamics*, Vol. 36, No. 6, 2013, pp. 1767-1771.
doi: 10.2514/1.55956

[3] Zhao, S., Gurfil, P., Zhang, J., "Optimal Servicing of Geostationary Satellites Considering Earth's Triaxiality and Lunisolar Effects", Journal of Guidance, Control, and Dynamics, Vol. 39, No. 10, 2016, pp. 2219-2231.
doi: 10.2514/1.G001424

[4] Zhang, J., Zhao, S., Yang, Y., "Characteristic Analysis for Elliptical Orbit Hovering Based on Relative Dynamics", IEEE Transactions on Aerospace and Electronic Systems, Vol. 49, No. 4, 2013, pp. 2742-2750.
doi: 10.1109/TAES.2014.6619962

[5] Colombo, C., Lucking, C., McInnes, C. R., "Orbital dynamics of high area-to-mass ratio spacecraft with J_2 and solar radiation pressure for novel Earth observation and communication services", *Acta Astronautica*, Vol. 81, 2012, pp. 137-150.
doi: 10.1016/j.actaastro.2012.07.009

[6] Budianu, A., Meijerink, A., Bentuma, M., J., "Swarm-to-Earth communication in OLFAR", *Acta Astronautica*, Vol. 107, 2015, pp. 14-19.
doi: 10.1016/j.actaastro.2014.10.041

[7] Colombo, C., Lucking, C., McInnes, C. R., "Orbit evolution, maintenance and disposal of SpaceChip swarms through electro-chromic control", *Acta Astronautica*, Vol. 82, No. 1, 2013, pp. 25-37.
doi: 10.1016/j.actaastro.2012.05.035

[8] McInnes, C. R., "An analytical model for the catastrophic production of orbital debris", *ESA Journal*, Vol. 17, 1993, pp. 293-305.

[9] Gor'kavyi, N., et al, "A new approach to dynamical evolution of interplanetary dust", *The Astrophysical Journal*, Vol. 474, 1997, pp. 496-502.
doi: 10.1086/303440

[10] Gor'kavyi, N., et al, "Quasi-stationary states of dust flows under Poynting-Robertson drag: New analytical and numerical solutions", *The Astrophysical Journal*, Vol. 488, 1997, pp. 268-276.

[11] McInnes, C. R., "A simple analytic model of the long term evolution of nanosatellite constellations", *Journal of Guidance, Control, and Dynamics*, Vol. 23, No. 2, 2000, pp. 332-338.
doi: 10.2514/2.4527

[12] Letizia, F., Colombo, C., Lewis, H., “Multidimensional extension of the continuity equation method for debris clouds evolution”, *Advances in Space Research*, Vol. 57, No. 8, 2015, pp. 1-17.
doi: 10.1016/j.asr.2015.11.035

[13] Colombo, C., McInnes, C. R., “Evolution of swarms of smart dust spacecraft”, New Trends in Astrodynamics and Applications VI, Courant Institute of Mathematical Sciences, New York, 2011.

[14] McInnes, C. R., “A Continuum Model for the Orbit Evolution of Self-propelled “Smart Dust” Swarms”, *Celestial Mechanics and Dynamical Astronomy*, Vol. 126, No. 4, 2016, pp. 501–517.

[15] Kozai, Y., “The motion of a close Earth satellite”, The Astronomical Journal, Vol. 64, 1959, pp. 367-377.

[16] Gurfil, P., Lara, M., “Motion near frozen orbits as a means for mitigating satellite relative drift”, *Celestial Mechanics and Dynamics and Astronomy*, Vol. 116, 2013, pp. 213-227.

[17] Zhang, J., Zhao, S., Zhang, Y., "Autonomous Guidance for Rendezvous Phasing Based on Special-Point-Based Maneuvers", Journal of Guidance, Control, and Dynamics, Vol. 38, No. 4, 2015, pp. 578-586.
doi: 10.2514/1.G000108

[18] Colombo, C., Xu, M., McInnes, C. R., “Stabilisation of the Hyperbolic Equilibrium of High Area-to-Mass Spacecraft”, 63rd International Astronautical Congress, Oct. 2-6 2012, Naples, Italy, IAC-12-C1.1.13.

[19] Hamilton, D. P., Krivov, A. V., “Circumplanetary Dust Dynamics: Effects of Solar Gravity, Radiation Pressure, Planetary Oblateness, and Electromagnetism”. *Icarus*, Vol. 123, 1996, pp. 503-523.

[20] Krivov, A. V., Sokolov, L. L., Dikarev, V. V., “Dynamics of Mars-Orbiting Dust: Effects of Light Pressure and Planetary Oblateness”, *Celestial Mechanics and Dynamical Astronomy*, Vol. 63, 1996, pp. 313-339.

[21] Krivov, A. V., Getino J., “Orbital Evolution of High-Altitude Balloon Satellites”, *Astronomy and Astrophysics*, Vol. 318, 1997, pp. 308-314.

[22] Kozai, Y., “Effects of Solar Radiation Pressure on the Motion of an Artificial Satellite”, *SAO Special Report*, Vol. 56, Part 3, 1961, pp. 25-34.

[23] Murphy, I .S., “Advanced Calculus”, Arklay Publishers, Stirling, 1984, pp. 79-101.